

Jet mixing optimization using machine learning control

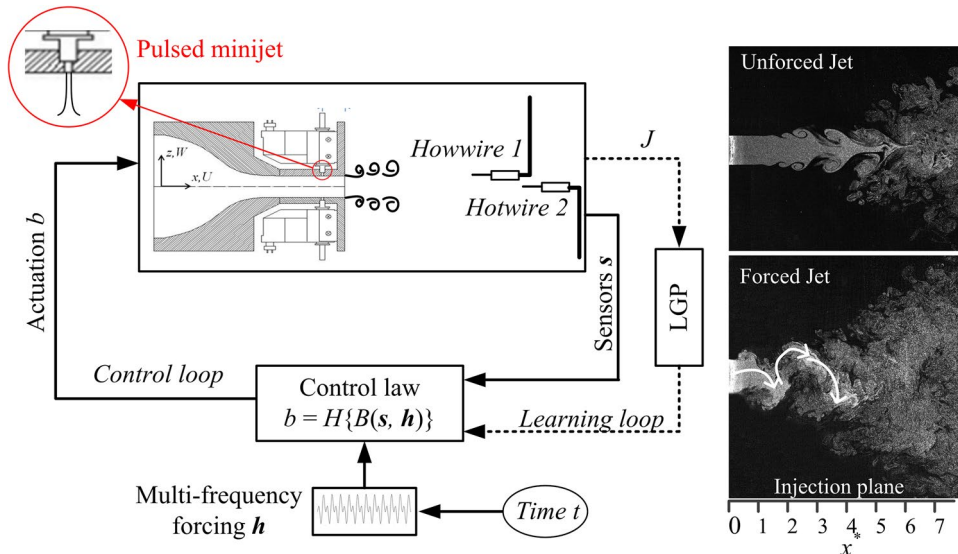
Zhi Wu^{1,2}  · Dewei Fan^{1,2} · Yu Zhou^{1,2} · Ruiying Li³ · Bernd R. Noack^{1,4,5}

Received: 2 February 2018 / Revised: 1 June 2018 / Accepted: 2 July 2018
© Springer-Verlag GmbH Germany, part of Springer Nature 2018

Abstract

We experimentally optimize mixing of a turbulent round jet using machine learning control (MLC) following Li et al. (Exp Fluids 58(article 103):1–20, 2017). The jet is manipulated with one unsteady minijet blowing in wall-normal direction close to the nozzle exit. The flow is monitored with two hotwire sensors. The first sensor is positioned on the centerline five jet diameters downstream of the nozzle exit, i.e. the end of the potential core, while the second is located three jet diameters downstream and displaced towards the shear-layer. The mixing performance is monitored with mean velocity at the first sensor. A reduction of this velocity correlates with increased entrainment near the potential core. MLC is employed to optimize sensor feedback, a general open-loop broadband frequency actuation and combinations of both. MLC has identified the optimal periodic forcing with small duty cycle as the best control policy employing only 400 actuation measurements, each lasting for 5 s. This learning rate is comparable if not faster than typical optimization of periodic forcing with two free parameters (frequency and duty cycle). In addition, MLC results indicate that neither new frequencies nor sensor feedback improves mixing further—contrary to many of other turbulence control experiments. The optimality of pure periodic actuation may be attributed to the simple jet flapping mechanism in the minijet plane. The performance of sensor feedback is shown to face a challenge for small duty cycles. The jet mixing results demonstrate the untapped potential of MLC in quickly learning optimal general control policies, even deciding between open- and closed-loop control.

Graphical abstract



Extended author information available on the last page of the article

1 Introduction

The enhancement of jet mixing is important to many industrial applications. One example is the production of polymers where additional substances are added in the main stream by jets and have to be rapidly mixed downstream. Similar mixing examples can be found in food industry. Another application is combustion in aeroengines: The first row of dilution jets enhances combustion by mixing while the second downstream row cools the fluid to prevent thermal damage to the turbine. Staying with aeroengines, the targeted homogeneous mixing of injected fuel in the airstream is affected by two-phase jet mixing. Aircraft carrier airplanes rely on enhanced jet mixing with flapping to prevent the burning of their tail after landing.

Consequently, jet mixing control has drawn significant attention in the past few decades. Jet mixing control can be classified into passive control and active control based on whether additional energy input is needed. For example, the use of non-circular nozzles (Gutmark and Grinstein 1999) or the deployment of tabs at the nozzle exit (Bradbury and Khadem 1975; Zaman et al. 1994) are passive control techniques. These devices can display impressive performance for the design conditions. Yet, the techniques are typically permanent fixtures which are not readily modified or removed. In addition, the control performance may deteriorate departing from the design condition. In contrast, the active control may potentially achieve higher performance for a large range of operating conditions. Examples are acoustic excitation (Zaman and Hussain 1980), plasma actuators (Samimy et al. 2007), synthetic jet (Ho and Gutmark 1987), oscillating boundaries based on piezo-electric actuators (Wiltse and Glezer 1993), steady and unsteady control jets (Davis 1982; Yang and Zhou 2016; Zhou et al. 2012). From an industrial perspective, actuators and sensors become increasingly more reliable and cheaper, i.e. more attractive for applications. Thus, active flow control enjoys increasing progress from many fronts, such as hardware development, control logic and modeling.

Active control techniques can be performed in an open-loop or closed-loop manner. By definition, closing the loop with sensors increases the opportunity space of actuation and—properly set up—should improve performance. The loop may be closed for in-time response to coherent structures or for adapting in response to changing flow conditions. Note that, ‘in-time’ means that the actuation responds on a time-scale much smaller than that of the physical process, while ‘adapting’ means that the change of the actuation parameter is slow as compared to the physical process time-scale (Brunton and Noack

2015). Many closed-loop control schemes have been proposed and investigated, as discussed in references Brunton and Noack (2015); Choi et al. (2008); Collis et al. (2004). Closed-loop control may be classified into model-based or model-free approaches, depending on whether the law is derived from a plant model or only based on the plant response.

Many computational flow control studies are based on local linearization of a Navier–Stokes based model. Linear models may be also identified in a black-box manner from input–output data sequences (Rapoport et al. 2003) or via a reduced-order model of the fluid dynamics (Choi et al. 2008). The challenge to this approach is the nonlinear dynamics of turbulence displaying a myriad of frequency-crosstalk mechanisms, like the change of the base flow by coherent structures or the turbulence cascade to smaller and smaller vortices with higher and higher frequencies. These important frequency crosstalk mechanisms are ignored in linear control strategies. They are also difficult to encapsulate in low-dimensional control-oriented models. This challenge motivates model-free control techniques which do not rely on a dynamical model of the fluid system. The majority of the experimental turbulence control studies rely on adaptive variations of one or few actuation parameters, such as the amplitude or frequency of suction or blowing. Examples include physics-based methods, such as Pastoor et al. (2008); Wu et al. (2016); Zhang et al. (2004b), extremum and slope-seeking control method (Becker et al. 2007; Brackston et al. 2016; Maury et al. 2012; Wu et al. 2015, 2016) and Machine Learning Control (MLC) (Brunton and Noack 2015; Duriez et al. 2016; Li et al. 2017) allowing for a very rich set of possible control laws. All approaches have been widely applied in turbulence experiments. For example, in the jet mixing enhancement with one pulsed minijet, extremum-seeking control (ESC) has been applied to obtain automatically and rapidly the optimal excitation frequency $f_{e,\text{opt}}$ of the minijet as monitored by the maximum decay rate K_{\max} of the jet centerline mean velocity. This ESC adapts a working open-loop control (Fan et al. 2017; Wu et al. 2016). Zhang et al. (2004a) used an in-time proportional-integral-derivative (PID) control to suppress the flow-induced vibration on a square cylinder by generating a very small cylinder surface oscillation, achieving a control performance which outperforms optimized open-loop control.

Hitherto, in-time turbulence control is a largely unexplored Terra Incognita. This is particularly true for jet mixing displaying a rich set of temporal and spatial scales. In this study, we seize this opportunity exploring a very rich set of control laws for jet mixing optimization—incorporating all major open- and closed-loop actuations. The recently discovered and enabled MLC framework has not yet been applied to this configuration.

In the current work, we optimize jet mixing with a single minijet actuator and two downstream hotwire sensors. As cost function, the averaged centerline velocity after the potential core is taken. For the control logic, we employ MLC based on linear genetic programming incorporating sensor-based feedback and multi-frequency forcing as well as combinations thereof. We follow a methodologically similar MLC study for drag reduction of an Ahmed body (Li et al. 2017). MLC significantly increases the range of possible control laws as compared to ESC. Moreover, MLC does not rely on the qualitative knowledge of steady-state maps and could find the global optimal value even when multiple extrema exist.

The manuscript is structured as follows. Section 2 describes the experimental setup. The control logic and associated MLC algorithm is outlined in Sect. 3. In Sects. 4 and 5, we detail the experimental control with sensor-based feedback and multi-frequency forcing, respectively. In Sect. 6 the mixing performance of different control schemes is physically explained. The conclusions in Sect. 7 summarize the MLC study and preview future developments.

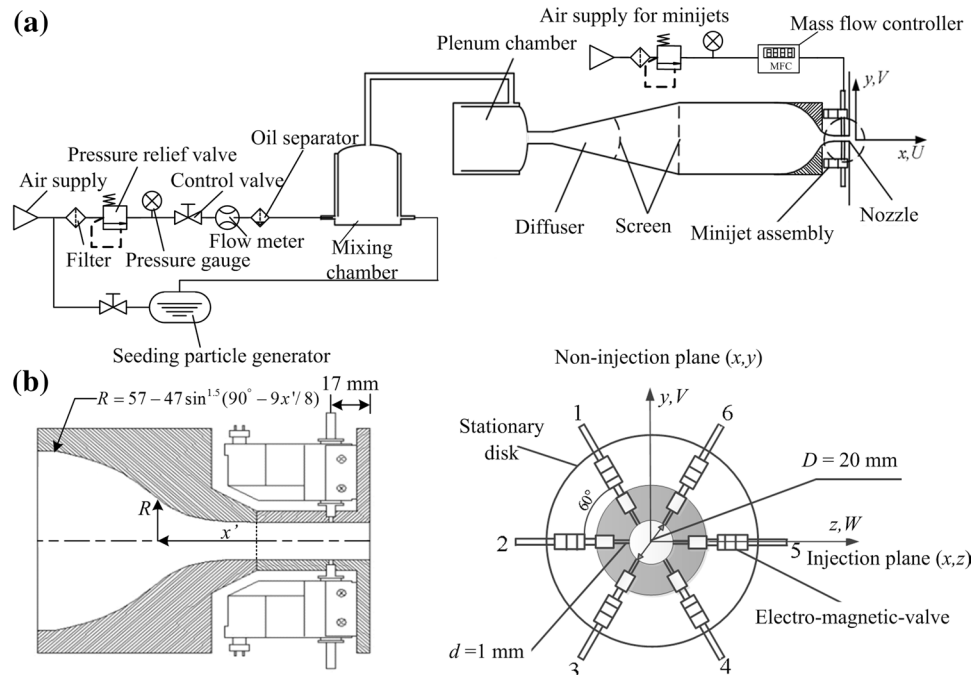
2 Experimental set-up

2.1 Jet facility and actuator system

The jet control platform, consisting of an axisymmetric main jet and a minijet assembly, is the same as that used in Fan et al. (2017). Figure 1a shows the schematic diagram of the air jet facility. The air for both main jet and minijet comes

from the same compressed air supply with a 12 bar gauge pressure. The compressed air first passes through a mixing chamber in the case of particle image velocimetry (PIV) or flow visualization measurements. After that, it passes through a tube, a plenum chamber, a 300 mm-long diffuser of 15° in half angle, two fine screens (7 mesh/cm) and a cylindrical settling chamber of 400 mm in length and 114 mm in the inner diameter. The nozzle contraction contour follows equation $R = 57 - 47 \sin^{1.5}(90^\circ - 9x'/8)$ (mm), as used in Zhou et al. (2012) and Wu et al. (2016). The nozzle was extended with a 47 mm-long smooth tube of diameter $D = 20$ mm. The Reynolds number $Re_D = U_j D / \nu$ of the main jet is fixed at 8000, where U_j is the jet centreline velocity measured at the exit of the nozzle extension and ν is the kinematic viscosity of air. Figure 1b shows the schematic diagram of the pulsed minijet assembly. There are six orifices of 1 mm in diameter drilled radially for the minijets, 17 mm upstream of the jet exit. To minimize the resistance, the orifices are suddenly expanded to a diameter of 4 mm before being connected via a short plastic tube to electromagnetic-valves (Koganei K2-100SF-09-LL), which are used to produce a pulsed minijet (Fig. 1b). The electromagnetic-valves can generate the pulsed jet in ON/OFF mode within the frequency range [0, 500] Hz. In the present study, we control only the ON/OFF of the electromagnetic-valves. The maximum frequency of the minijet is 500 Hz, exceeding $3f_0$ at $Re_D = 8000$, where $f_0 = 135$ Hz is the dominant frequency of the uncontrolled jet. Only one single minijet injection was investigated presently. The mass flow rate of the minijet varied via a mass flow controller (FLOWMETHOD FL-802) with a range of 7 Standard Liter Per Minute (SLPM), whose

Fig. 1 Schematic of the experimental setup: **a** main-jet assembly; **b** minijet assembly



experimental uncertainty is no more than 1%. The mass flow rate of the minijet is fixed at 1.3 l/min for all the current investigations, corresponding to $C_m = 1.2\%$, where the C_m is the mass flow rate ratio of the main jet to the minijet.

The origin of the coordinate system is defined at the centre of the jet exit, with the x - and z -axes along the streamwise and the radial minijet directions, respectively, and the y -axis is normal to the (x, z) plane, following the right-hand rule. The (x, z) and (x, y) planes are hereinafter referred to as the injection and non-injection planes, respectively. In this paper, an asterisk superscript denotes normalization by D or/and U_j . For example, $x^* = x/D$, $u^* = u/U_j$.

In this paper, we mainly focus on the optimization of the control logic for driving electro-magnetic valves. The control performance is strongly related to the penetration depth of the minijet. The penetration depth depends on both C_m and duty cycle (DC). A parametric study has provided a local maximum of jet mixing decay rate at excitation frequency $f_e = 67$ Hz, $DC = 7\%$ and $C_m = 1.2\%$. Currently, the experiment only allows slow changes of C_m over hundreds of actuation periods. In this study, we have fixed C_m at the optimal value. In an ongoing investigation, the optimization of C_m is included in machine learning control. It should be noted that C_m is a steady parameter and constitutes an add-on to genetic programming.

Given a fixed C_m , the DC is directly correlated with the blowing ratio between the minijet and the main jet. For a better understanding of the influence of the unsteady minijet on the initial conditions of the main jet, following Zhou et al. (2012), we placed a single hotwire upstream of the main jet exit at $x^* = -0.85$ ($y^* = 0$ and $z^* = -0.35$), where the minijet is excited at $DC = 0.1, 0.4$ and 1 ($C_m = 1.2\%$, $f_e = 67$ Hz). The hotwire is oriented such that it can measure the W signal in the absence of the main jet. The W^* signal

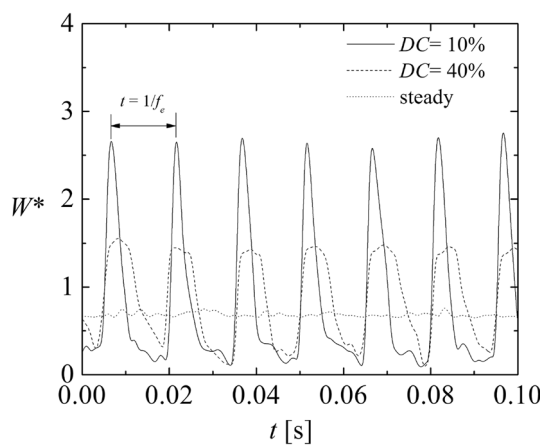


Fig. 2 Time histories of streamwise fluctuating velocity W in the absence of the main jet measured at $(x^*, y^*, z^*) = (-0.85, 0, -0.35)$ for $C_m = 1.2\%$, $f_e/f_0 = 0.5$

(Fig. 2) exhibits different behaviors as DC varies, where $W^* \approx 0$ and significantly above 0 correspond to the off- and on-states of the minijet, respectively. Given $C_m = 1.2\%$ and $f_e = 67$ Hz, W^* displays sharp peaks in the on-state, which are periodic and clearly separated for $DC = 0.1$. However, the peaks appear less pronounced at $DC = 0.4$. The more pronounced peak in W^* for $DC = 0.1$ than for $DC = 0.4$ implies a higher penetration depth at smaller DC , as reported by Johari et al. (1999) for the pulsed jet in cross flow.

2.2 Velocity measurement and flow visualization facilities

Two tungsten wires of $5\text{ }\mu\text{m}$ in diameter, operated on a constant temperature circuit (Dantec Streamline) at an overheat ratio of 1.8, are placed at $(x^*, y^*) = (3, 0.25)$ and $(5, 0)$ to measure the streamwise velocities u_{3D} and u_{5D} , respectively.

Note that the slight deviation from centreline for hotwire 1, which is for measuring the u_{3D} , is used to monitor the shear-layer vortices, along with preventing its influence on hotwire 2. The output signal of the hotwire anemometer is offset, amplified, and filtered at a cut-off frequency of 500 Hz before being digitized and saved in a PC by a *National Instruments* multifunction I/O Device (PXIE-6356). The sampling frequency is 1 kHz for all experiments. The hotwires were calibrated at the jet exit using a pitot tube and a micromanometer (Furness Controls FCO510). The experimental uncertainty of the hotwire measurement is estimated to be less than 2%.

A planar high-speed PIV system, including a high speed camera (LaVision ImagerproHS4M, 2016×2016 pixels resolution) and pulsed laser source (Litron LDY304-PIV, Nd:YLF, 120 mJ/pulse) is deployed for flow visualization in the (x, z) and (x, y) planes. An oil droplet generator (TSI MCM-30) is used to generate fog for seeding flow. The seeding particles are supplied into the mixing chamber (Fig. 1a) to mix with air. Flow illumination is provided by a laser sheet of 1 mm in thickness generated by a pulsed laser source of 120 mJ via a cylindrical lens. Particle images are captured at a sampling rate of 250 Hz.

2.3 Real-time system

The real-time control is realized by a *National Instrument* PXIE-6356 multifunction I/O Device running at a sampling rate of $F_{RT} = 1$ kHz, where a LabVIEW Real-Time module is used to process the program. Sensor data acquisition and control command generation for open- and closed-loop control are performed at the same sampling rate. For the effective working of the actuator, a verification is performed before sending the command to the actuators to ensure that the ON/OFF command lasts at least 1 ms.

The available periodic frequencies f consistent with F_{RT} can be derived from $f = F_{\text{RT}}/N_{\text{sp}}$, where N_{sp} is the number of sampling points in one time period $1/f$. The working frequency range of actuators ([0, 500] Hz) imposes a minimum value for N_{sp} , being $N_{\text{sp}} \geq 2$. For a given f , the possible duty cycle DC can be deduced from $DC = m/N_{\text{sp}}$, $m = 1, \dots, N_{\text{sp}} - 1$. The value of m starts from 1 and ends at $N_{\text{sp}} - 1$ to ensure a response time of 1 ms for an effective working of the actuators. Thus, the number of possible duty cycles N_{DC} for a given f is $N_{\text{DC}} = N_{\text{sp}} - 1 = F_{\text{RT}}/f - 1$, which increases with N_{sp} and decreases with f . This process is similar to that used in Li et al. (2017).

Figure 3 displays the permitted frequencies and duty cycles and shows the manually selected frequencies which allow for a locally maximum number of duty cycles. The number of possible duty cycles decreases as the frequency increases due to the limited sampling points in one period. Note that Fig. 3 includes all the possible DC and f within the range [10, 500]. The red filled circles highlight the selected periodic forcing cases considered in the following, which contain the most interesting frequency range [20, 200] Hz.

3 Machine learning control (MLC)

The mixing enhancement of a turbulent jet involves a large range of temporal and spatial scales with complex nonlinear interactions. Model-based control as used for the stabilization of steady laminar flows faces fundamental challenges for such turbulent flow and has, to the best of the authors' knowledge, not been presented for experimental mixing

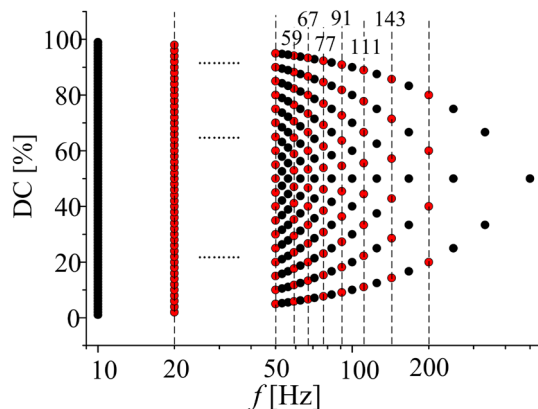


Fig. 3 Frequency selection for the multi-frequency forcing ansatz (5). Each circle corresponds to a frequency and duty cycle achievable with a $F_{\text{RT}} = 1$ kHz data acquisition system. The horizontal lines and numbers indicate the selected frequencies for harmonic inputs. Red dots highlight the cases considered in this study. Black dots represent other combinations of f and DC consistent with F_{RT} . Combinations between [10 20]Hz and [20 50]Hz are not explicated for reasons of figure clarity. See Fig. 3 of Li et al. (2017) for a comparison with similar selection process

enhancement of turbulence. Instead, we follow Dracopoulos & Kent's pioneering work (Dracopoulos and Kent 1997), in which control design is framed as regression problem and solved with one of the most powerful method of machine learning: genetic programming. This strategy, referred to as *Machine Learning Control (MLC)* in recent literature (Brunton and Noack 2015; Duriez et al. 2016), has been applied with large success for a range of turbulence control experiments (Noack 2017). MLC has continually outperformed existing control strategies often exploiting surprising nonlinear frequency cross-talk mechanisms.

In this section, the employed MLC implementation is described. First (Sect. 3.1), the control problem is framed as optimization of a cost function. Then (Sect. 3.2), a general control ansatz is proposed. This ansatz comprises nonlinear sensor-feedback with signal history, multi-frequency forcing and combinations thereof. Now, the search for an optimal control law can be formulated as regression problem (Sect. 3.3). Finally (Sect. 3.4), the employed linear genetic programming is detailed as powerful regression solver, including the parameters of this evolutionary algorithm.

3.1 Cost function

Good jet mixing is associated with large entrainment of the ambient flow into the high-momentum jet fluid emanating from the orifice. This entrainment reduces the streamwise velocity on the centerline. Following earlier work (Wu et al. 2016), we take the streamwise velocity u_{5D} five jet diameters downstream as mixing indicator. This location is approximately at the end of the potential core. The smaller this velocity, the better the mixing between the high-momentum jet and the surrounding ambient fluid. In the cost function, the centerline velocity is normalized by the maximum jet velocity at the orifice

$$J = \frac{\overline{u}_{5D}}{U_j}. \quad (1)$$

Here, the overbar denotes a time average. This non-dimensionalization allows comparing jet mixing for a range of operating conditions. The minimization of the cost function corresponds to the maximization of the jet centerline decay rate,

$$\overline{K} = \frac{U_j - \overline{u}_{5D}}{U_j} = 1 - J. \quad (2)$$

The mean axial velocity is usually chosen as a quantitative measure of the effect of the forcing on the jet development (e.g., Freund and Moin 2000; Yang et al. 2016). Following Hussain and Husain (1989) and Mi et al. (2007), Zhou et al. (2012) defined in their investigation of jet

manipulation using two steady minijets an equivalent jet width $R_{eq} = [R_H \times R_V]^{1/2}$, where R_H and R_V were the half-widths of the mean velocity distributions in the (x, z) and (x, y) planes, respectively. Apparently, R_{eq} is a better indicator of the overall spread of the jet than either R_H or R_V . They found that R_{eq} was correlated approximately linearly with the centerline velocity decay rate \bar{K} , as defined in Eq. (2). We characterize the jet entrainment rate by \bar{K} building on these studies.

We expect that the observed asymmetric flapping forcing is highly efficient in terms of other mixing characterizations, e.g. diffusion of temperature of a hot jet. Yet, MLC may yield other control laws for other cost functions or other actuators. The one-point hotwire measurement of the cost J is very convenient for experiment. In computational studies, the width of the jet may be more appropriate and robust (Hilgers and Boersma 2001; Koumoutsakos et al. 2001).

3.2 Ansatz for control law

We search to optimize actuation in a very general ansatz for the control law comprising, for instance, multi-frequency forcing and sensor-based feedback with signal history. In the following the actuation command is denoted by b . It can take binary values 1 and 0 depending on whether minijet is on or off. The actuation induced by the minijet is a pulsed jet whose maximum velocity scales approximately with the inverse of the duty cycle.

3.2.1 Multi-frequency forcing

In similar experiments (Fan et al. 2017), a periodic forcing with a frequency $\omega^* = 2\pi f^*$, $f^* \approx 67$ Hz was found to be very effective. The corresponding open-loop control law reads

$$b(t) = H(\cos(\omega^* t) - k), \quad (3)$$

where H represents the Heaviside function and k controls the duty cycle. The larger $k \in (-1, 1)$, the smaller the duty cycle. Following Li et al. (2017), a much more general multi-frequency forcing is considered, generated here by 9 harmonic functions $h_i = \cos(2\pi f_i t)$, $i = 1, \dots, 9$. The frequencies are selected based on the data acquisition frequency of 1 kHz. With finite data acquisition frequency, only discrete frequencies with discrete duty cycles are possible as displayed in Fig. 3.

We comprise the harmonic functions into a vector-valued frequency generator

$$\mathbf{h}(t) = [h_1 \ h_2 \ \dots \ h_9]^\dagger \quad (4)$$

where the \dagger superscript denotes the transpose, $h_i = \cos(2\pi f_i t)$, and $f_i = 20, 50, 59, 67, 77, 91, 111, 143, 200$ Hz for $i = 1, \dots, 9$, respectively. We do not include sinusoidal

functions at the same frequencies. In the open-loop actuation literature, phase differences are only found to be important for few frequency ratios, e.g. harmonic and subharmonic components of the mixing layer (Monkewitz 1988). Most Lissajous figures with h_i, h_j densely fill out the square $[-1, 1] \times [-1, 1]$, indicating the phase difference cannot be expected to have an effect. The open-loop multiple forcing actuation is performed with

$$b(t) = B(\mathbf{h}(t)). \quad (5)$$

If B were a linear function—putting the binary nature of actuation aside—the resulting actuation command can exhibit the input frequencies. If B were a pure quadratic function, all different frequencies may appear. In case of a general nonlinear function, a large range of frequencies can be generated. For instance, $h_1^{10} - 1/2$ generates a harmonic function with frequency $10f_1$. Hence, the main frequency limitation of the general ansatz (5) is not caused by the ansatz but by the actuator performance.

3.2.2 Sensor-based feedback

The considered feedback is based on the hot-wire signal u_{5D} used for the cost function (1) and on the slightly displaced hot-wire measurement three diameters downstream u_{3D} monitoring the shear-layer vortices. The feedback signals are based on the Reynolds decomposition into a one period average denoted by $\langle \cdot \rangle_T$ and a fluctuation, $u_{5D} = \langle u_{5D} \rangle_T + u'_{5D}$ and $u_{3D} = \langle u_{3D} \rangle_T + u'_{3D}$. The average is based on a sliding window with the forcing period T corresponding to the best excitation frequency 67 Hz. In addition, the signals are normalized by the jet velocity at the nozzle exit to arrive at more robust control laws for a range of operating conditions, e.g. different jet velocities. The resulting feedback argument reads

$$\mathbf{s}(t) = \begin{bmatrix} s_1(t) \\ s_2(t) \\ s_3(t) \\ s_4(t) \end{bmatrix} = \frac{1}{U_j} \begin{bmatrix} u_{3D}(t) \\ u_{5D}(t) \\ u'_{3D}(t) \\ u'_{5D}(t) \end{bmatrix}. \quad (6)$$

Note that $J = \overline{s_2}$.

The ansatz for the sensor-based feedback law has the form:

$$b(t) = B(\mathbf{s}(t)). \quad (7)$$

3.2.3 Generalized feedback control

A natural generalization of the previous approaches reads

$$b(t) = B(\mathbf{s}(t), \mathbf{h}(t)). \quad (8)$$

The sensor-based feedback might, for instance, control the duty cycle of an actuation frequency. In Sects. 4 and 5, we

will explore jet mixing performance for a variety of control laws.

3.3 Control design as model-free regression problem

The cost function J evidently depends on the chosen control logic $B(\mathbf{s}, \mathbf{h})$. We search for a control law which minimizes J ,

$$B^* = \arg \min_B J[B(\mathbf{s}, \mathbf{h})]. \quad (9)$$

The model-free optimization of control laws (9) is a difficult regression problem of the second kind, like in a variational problem: For a given argument (sensor signal) the optimal actuation command is generally not known. The performance can only be judged from the complete mapping and its long-term behavior in the plant. Genetic programming has a demonstrated capability to solve such problems of variational kind. In addition, no structure of the control law needs to be assumed.

In contrast, artificial neural networks are typically applied to regression problems of the first kind, where the optimal output is already known for each input argument. Evidently, learning the correct mapping is significantly simplified by this advance information. In Lee et al. (1997), for instance, the artificial neural network has learned sensor-based feedback from a known full-state feedback. This optimal control law was derived from the Navier–Stokes equations. In experiments, we typically do not have the luxury of a priori known full-state feedback.

The optimization of multi-frequency open-loop forcing is a regression problem of the second kind, as the effect of this forcing is the result of long-term nonlinear interactions of the flow. The application of a larger spectrum of regression techniques in turbulence control have been reviewed in Brunton and Noack (2015).

3.4 Linear genetic programming as regression solver

Following Li et al. (2017), the control optimization problem (9) is solved using *linear genetic programming* (LGP). LGP is a powerful regression technique of machine learning which can optimize general nonlinear mappings, such as the control law. We refer to the exquisite textbook of Wahde (Wahde 2008) for a quick overview on a spectrum of evolutionary algorithms including LGP, to the detailed LGP textbook by Brameier and Banzhaf (2007) and to the first turbulence control applications (Li et al. 2017). In this section, LGP is sketched and the key parameters are listed.

LGP control starts like a Monte–Carlo approach with I random control laws, referred to as *individuals*:

$$b = B_i^{(1)}, \quad i = 1, \dots, I. \quad (10)$$

The superscript (1) represents the first generation. The jet mixing experiment grades the performance of each law $J^{(1)}$ in the plant. Figure 4 shows the plant, the fast inner control loop and the slow outer evaluation/learning loop. Then, the individuals are re-numbered and ranked in the order of performance,

$$J_1^{(1)} \leq J_2^{(1)} \leq \dots \leq J_I^{(1)}. \quad (11)$$

The best N_e individuals are adopted in the new generation,

$$B_i^{(2)} = B_{i-}^{(1)}, \quad i = 1, \dots, N_e. \quad (12)$$

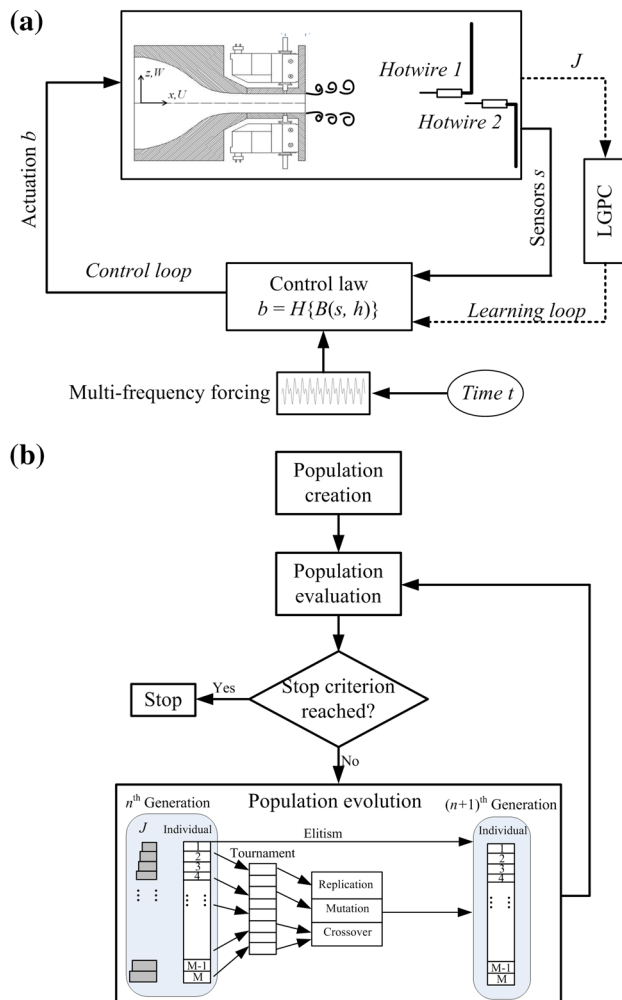


Fig. 4 Principle sketch of machine learning control. **a** The fast inner control loop with the jet mixing plant and the slow outer evaluation/learning loop. **b** The evolutionary algorithm behind the learning of the best control law

This operation is called *elitism*. The remaining $I - N_e$ individuals of the new generation are determined with a random sequence of three genetic operations: *crossover*, *mutation*, and *replication* with probabilities P_c , P_m and P_r , respectively. Crossover has two arguments (individuals) and breeds two new individuals exchanging equally sized part of ‘genes’ from both individuals. This operation tends to yield better individuals, e.g. *exploit populated local minima*. Mutation has a single argument and replaces part of the ‘genes’ rather randomly. This operation might *explore new local minima*. Replication has one argument which is copied unaltered into the new generation. Evidently, this operation has a memory effect. The argument of these operations is decided in a tournament. N_t individuals of the graded generations are chosen with equal probability for the tournament. The genetic operation takes the best or the best two individuals, i.e. there is a bias towards processing better individuals but low performing individuals are not completely ignored.

These iterations are performed until convergence of the best performing individuals or the end of the measurement time is reached (see Fig. 4b). Let N_g be the number of the evaluated generations before termination. The best control law of the last generation $B_1^{(N_g)}$ is taken as the solution of the regression problem (9).

In LGP, each individual consists of a set of instructions using elementary operations on a register r_j , $j = 1, \dots, N_s + N_b + N_c$, with the first N_s values for the input signals, the next $N_b = 1$ values for the actuation commands, and N_c constants. For sensor-based feedback (7) there are four input signals $N_s = 4$, for multi-frequency forcing (5) $N_s = 9$ and for the generalized feedback (8) $N_s = 4 + 9 = 13$. Before any operation, the input registers are initialized with the argument values and the actuation register is zeroed. The k th instruction is coded as integer matrix B_{kl} , $l = 1, \dots, 4$. Here, B_{k3} denotes the index of the operation, e.g. ‘1’ for ‘+’, B_{k1} , B_{k2} represents the index of the input registers and B_{k4} represents the index of the output registers (excluding

the constants). Thus, $B_{k1} = 2$, $B_{k2} = 3$, $B_{k3} = 1$ and $B_{k4} = 5$ corresponds to $r_5 = r_2 + r_3$.

The employed parameters of LGP are listed in Table 1. The same or very similar parameters have been chosen in dozens of other turbulence control experiments, flow control simulations or dynamical systems control (Duriez et al. 2016). The performance of the resulting machine learning control was not critically dependent on any of these parameters.

4 Sensor-based feedback optimized with MLC

In this section, a sensor-based feedback control using MLC (8) is investigated. Experiments are performed at $Re_D = 8000$ and $C_m = 1.2\%$. The C_m of 1.2% corresponds to the optimum jet mixing performance (Wu et al. 2018). Figure 5a shows the evolution of the cost $J_i^{(n)}$ as function of the individual index $i = 1, \dots, 100$ for 6 generations

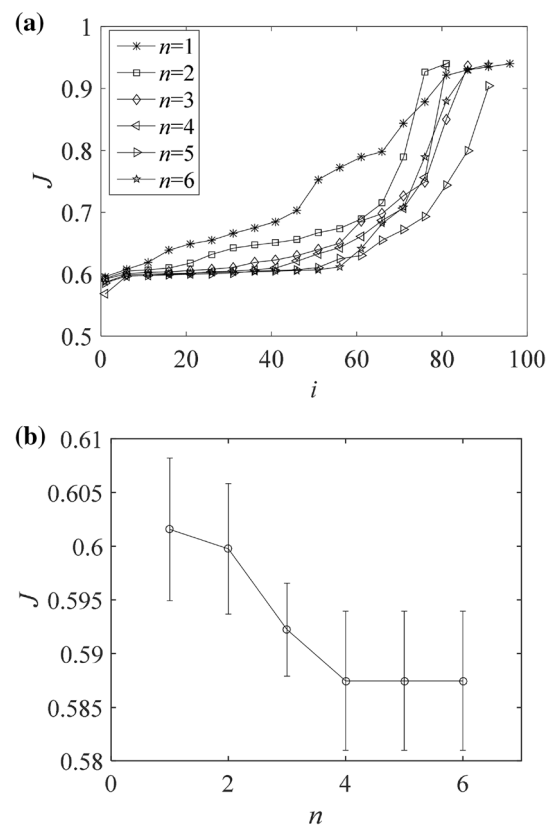


Fig. 5 Learning of the sensor-based feedback with MLC. **a** Evolution of the cost J versus the individual index $i = 1, \dots, 100$ for 6 generations $n = 1, \dots, 6$. For visual clarity, only every fifth individual is plotted, i.e. $i = 1, 6, 11, \dots, 96$. **b** Cost of the optimal individual in the 6 generations $J_1^{(n)}; n = 1, \dots, 6$. The circles correspond to the averaged J values and the error bars mark the standard deviation of repeating evaluations of the optimal control law

Table 1 LGPC parameters in the experiments

Parameters	Value
Population size	$I = 100$
Elitism	$N_e = 1$
Crossover	$P_c = 70\%$
Mutation	$P_c = 20\%$
Replication	$P_c = 10\%$
Operations	+, -, ×, ÷, x^2 sin, tanh, log, exp
Constants	$N_c = 6$
tournament	$N_t = 7$
Constant range	$[-1, 1]$

($n = 1, \dots, 6$). For visual clarity, only every 5th data is displayed, i.e. $i = 1, 6, 11, \dots, 96$. The individuals of each generation are ordered by J value following (11). Here, $i = 1$ corresponds to the smallest J and the best control law. For the first generation $n = 1$, J increases gradually with i starting from the minimum of $J_1^{(1)} \approx 0.6$. With increasing number of generations, the curve converges to a plateau for the first half of the individuals. Genetic algorithm breeds more and more similar or even identical individuals with every generation. At some point, the learning is converged while the last half of the individuals explore other new control laws but fail to find better minima.

This convergence is depicted in Fig. 5b showing the performance $J_1^{(n)}$ of the best individual for each generation $n = 1, \dots, 6$. At $n \geq 4$ the J value is converged to 0.588 corresponding to a decay rate of $\bar{K} = 1 - J \approx 0.412$. At $n = 6$ the evolution is stopped and the best individual of the last generation b_{opt} is taken as MLC law:

$$b_{\text{opt}} = H(-s_3) \quad (13)$$

The actuation fires when the streamwise velocity of the shear-layer sensor at $x/D = 3$ is below the average. Equation (13) is the simplified version of the equivalent LGP algorithm $b_{\text{opt}} = H(0.752s_3/(-0.576))$. The error bar in Fig. 5b displays the standard deviation of the repeated tests of the best control law in all the generations. The error bar significantly decreases with increasing time window. For MLC, only the approximate relative ordering needs to be preserved and we save significant measurement time using a 5 s time window.

The MLC feedback forcing (13) leads to nearly periodic forcing as displayed in Fig. 6. The unforced s_1 signal from the shear-layer sensor (Fig. 6a) displays a dominant periodicity at $f_0 = 135 \text{ Hz}$. This frequency corresponds to the coherent shear-layer structures. The forcing leads to a much lower frequency of 55 Hz corresponding to a flapping. This flapping frequency dominates the behavior of the shear-layer sensor at $x/D = 3$ and is also visible in the reading of the centerline sensor at $x/D = 5$. Note that s_3 follows s_1 modulo the short-time averaged mean value. Ditto for s_4 and s_2 . The actuation fires for short periods of time when s_3 is negative following (13) (see Fig. 6b). In other words, the actuation fires whenever the control law (13) is larger than the threshold value Th (see Fig. 6d, e).

The MLC discovery of s_3 as actuation trigger is visualized in Fig. 7. This graph represents the percentage P_{si} of having s_i in the expression of all I control laws for each generation n . With increasing number of generations n , the dominance of s_3 becomes more pronounced. In the last generation, s_1, s_2 and s_4 are neglected in most individuals as control law input. Note that multiple appearances of s_3 in one individual are counted only once. This behavior is easily explained by the high efficiency of periodic forcing for jet mixing via flapping

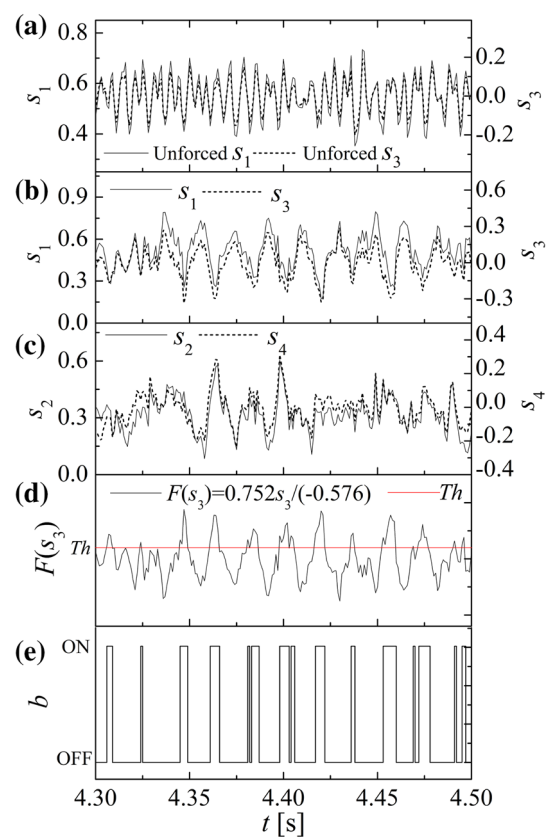


Fig. 6 Sensor-based feedback of MLC—time histories. The instantaneous unforced signal s_1 and s_3 (a), forced signals s_1-s_4 (b, c), signal of the best control law (13) (d) and the corresponding control signals b (e)

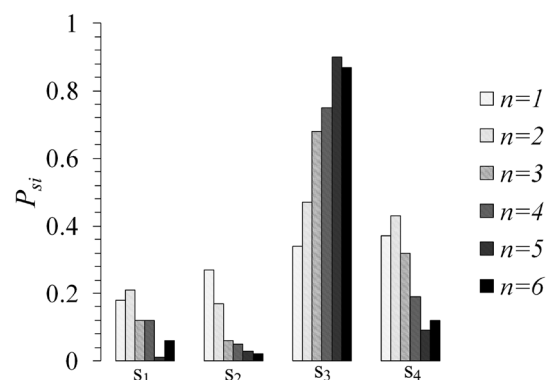


Fig. 7 Sensor-based feedback of MLC—learning of the sensor selection. For each generation $n = 1, \dots, 6$, we represent the percentage P_{si} of having s_i in the expression of all I control laws for each generation n

and by the higher sensitivity of the shear-layer sensor to this frequency.

The convergence of the learning process is displayed in Fig. 5. Following Kaiser et al. (2017), we also want to learn

the ‘control landscape’ of all tested individuals employing a proximity map. For that purpose, we rely on Multi Dimensional Scaling (MDS) (Mardia et al. 1979), a method classically used to visualize high-dimensional data in a low-dimensional feature space. Specifically, we employ classical multidimensional scaling (CMDS) which is originated from the works of Schoenberg (1935) and Young & Householder (1938) and optimally preserves the distances between the data in the projection from a high-dimensional space to a low-dimensional feature space. Our infinite-dimensional objects are $N = I \times 6 = 600$ control laws. The control laws are indexed in order of appearance, i.e. $i = 1, \dots, 100$ belong to the first generation, $i = 101, \dots, 200$ refer to the second generation, and so on. Next, we need to quantify the relative configuration of control laws with a distance matrix $D = (D_{lm})_{1 \leq l, m \leq N}$. Here, D_{lm} denotes the difference between individuals l and m . The square of the distance matrix D^2 is defined by

$$D_{lm}^2 = \left\langle |b_l(s) - b_m(s)|^2 \right\rangle_{l,m} + \alpha |J_l - J_m| \quad (14)$$

The first term represents the difference between the l th and m th control laws averaged over the sensor readings of both actuated dynamics. Thus, the averaging takes into account the frequency and relevance of the sensor reading. The second term penalizes the difference of their achieved costs J with coefficient α . This penalization smoothes the control landscape, i.e. the visualization of the cost J in the feature space. The penalization parameter α is chosen so that the maximum variation of the first and second term of (14) are equal. Thus, the dissimilarities between control laws and between the cost functions have comparable weights in the distance matrix D_{lm} . For further details, please refer to Duriez et al. (2016). The aim of CMDS is to find a centred representation of points $\Gamma = [\gamma_1, \gamma_2, \dots, \gamma_N]$ with $\gamma_1, \gamma_2, \dots, \gamma_N \in \mathbb{R}^2$, such that the pairwise distances of the feature points are—in a well-defined sense—optimally close to the original distances, i.e. $\|\gamma_l - \gamma_m\|_2 \approx D_{lm}$.

Figure 8 shows the proximity map of all control laws ($N = 600$) in a two dimensional plane $(\gamma^1, \gamma^2) \in \mathbb{R}^2$ and the power spectral density of the selected control laws $A-L$, respectively. The γ^1 and γ^2 represent the coordinates in the two dimensional plane. Each dot represents one control law and the corresponding J value is color-coded. The optimal law b_{opt} is indexed by G . All individuals are close to a V-shaped curve except continuous blowing with duty cycle $DC = 1$ as isolated point A . On the curve, the DC increases constantly from 0 to 94.5% for control laws B to L . The second feature coordinate γ^2 clearly correlates with the DC of the control signal. The first feature coordinate γ^1 appears to correlate with spectral characteristics. The maximum frequency of the best performing law G is on the rightmost side of the curve while the other individuals have lower dominant

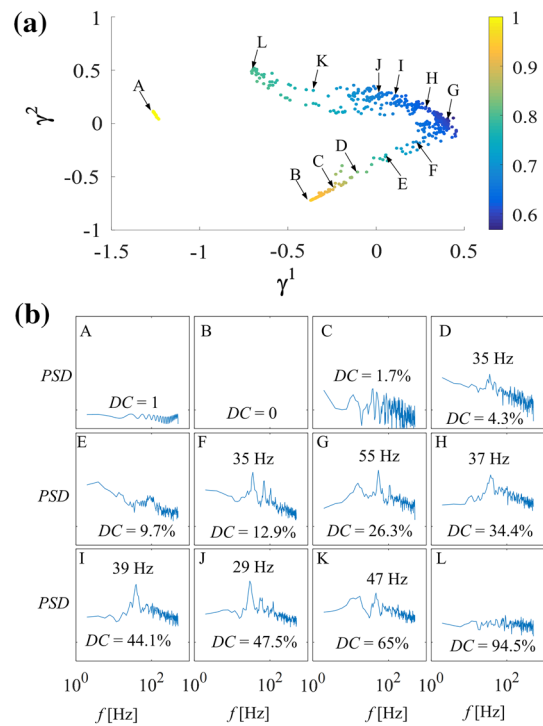


Fig. 8 Proximity map of all tested control laws for sensor-based feedback with MLC. **a** Visualization of (dis)similarity associated with the entire collection (600 individuals) of the sensor-based feedback control laws. Each dot represents an individual control law and the distance between two control laws approximates their respective dissimilarity. The color scheme represents the J value. The best performing individual is indicated by G . **b** The corresponding power spectrum and duty cycles of control laws $A-L$

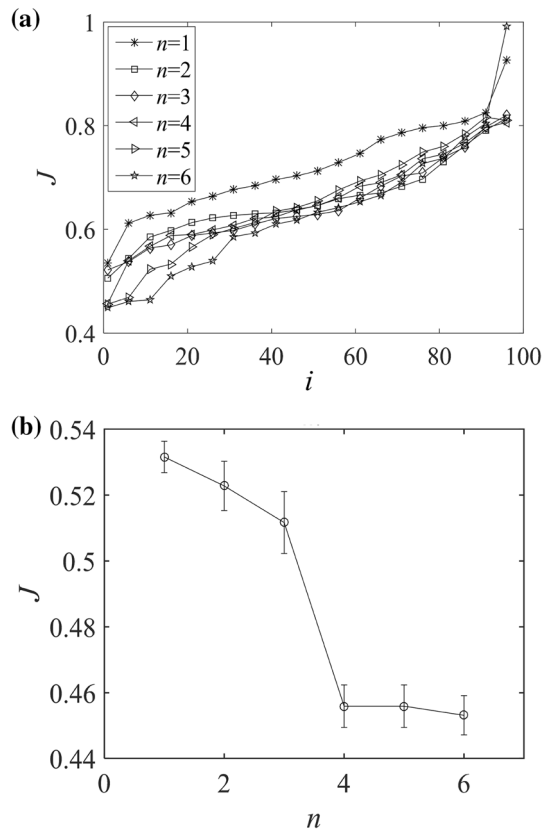
frequencies. The proximity map reveals that MLC explores multi-frequency actuation mechanisms and arrives at a dominant periodicity with low duty cycle of 26.3% and new flapping frequency of 55 Hz. This frequency of 55 Hz does not equal the optimal frequency (i.e. 67 Hz) achieved using periodic forcing method (Fan et al. 2017). One possible reason is the influence of turbulence, which makes it difficult for sensor-based feedback control methods to search for the optimal frequency and duty cycle. Detailed discussion will be given in Sect. 6.2.

5 Multi-frequency forcing optimized with MLC

The sensor-based feedback control results distill nearly periodic forcing as best actuation. However, the possibility of feedback control to give rise to strict periodic forcing is mitigated by the low-frequency drifts and high-frequency noise. Moreover, in some MLC studies, open-loop multi-frequency

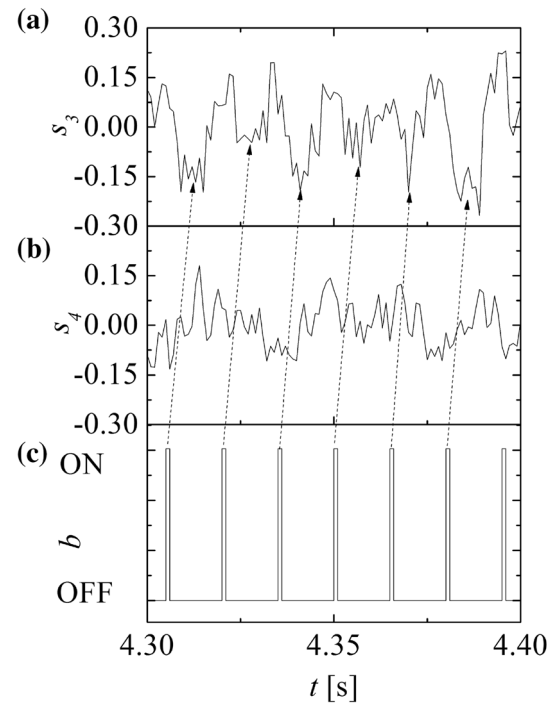
Table 2 Frequencies of the harmonic functions $h_i(t) = \cos(2\pi f_i t)$ used as inputs for the MLC law yielding multi-frequency actuation

h_i	h_1	h_2	h_3	h_4	h_5	h_6	h_7	h_8	h_9
f_i [Hz]	20	50	59	67	77	91	111	143	200

**Fig. 9** Learning multi-frequency actuation with MLC. The cost function $J_i^{(n)}$ is displayed like in Fig. 5

forcing has been shown to outperform both periodic forcing and sensor-based feedback (Li et al. 2017). This motivates the use of MLC to optimize open-loop multi-frequency actuation. Here, a range of harmonic functions are used as inputs of control laws. Table 2 provides the chosen harmonic functions $h_i(t)$.

Figure 9a illustrates the evolution of the cost J as function of the individual index i for 6 generations. As for the sensor-based feedback, we plot only every 5th individual for visual clarity. Interestingly, the increase of J with i is steeper than that for the sensor-based feedback, indicating that the minimum is less populated. One reason may be that the number of control law arguments has more than doubled and the search space is in some vague sense ‘larger’. Another reason is that the harmonic functions are by construction less correlated than the sensor signals. This reduced correlation has frequently been found to be associated with the increase of learning time. A particularly noteworthy characteristic

**Fig. 10** Multi-frequency forcing with MLC—time histories. The instantaneous sensor signals s_3 (a), s_4 (b) and control signals b (c) are displayed for the best control law (15)

of this MLC run is the sudden jump of the best cost value $J_1^{(n)}$ from 0.510 to the converged value of $J_1^{(4)} = 0.458$ in the fourth generation (Fig. 9b), indicating that a new minimum may have been found from generation 3 to 4. This value is 24% better than 0.588 of the sensor-based feedback, and corresponds to a decay rate of $\bar{K} = 0.542$. The error bars of open- and closed-loop MLC are similar to each other.

The resulting MLC law reads

$$b_{\text{opt}} = H \left(\log \left| \left(-0.646 - \log(|h_4|)^2 \right) \right| \right) \quad (15)$$

and corresponds to periodic forcing with a frequency of $f_e = 67$ Hz and a duty cycle of 7%. Figure 10 illustrates the corresponding actuation command and the resulting sensor fluctuations in the shear layer (s_3) and on the centerline (s_4) in a few period interval. The actuation lines up fairly well with positive s_3 values. Nevertheless, there is an inherent time delay (≈ 0.01 s) between the actuation and s_3 signal due to the response time of the flow field to the actuation signal. Thus, the actuation is correlated to low s_3 values as indicated

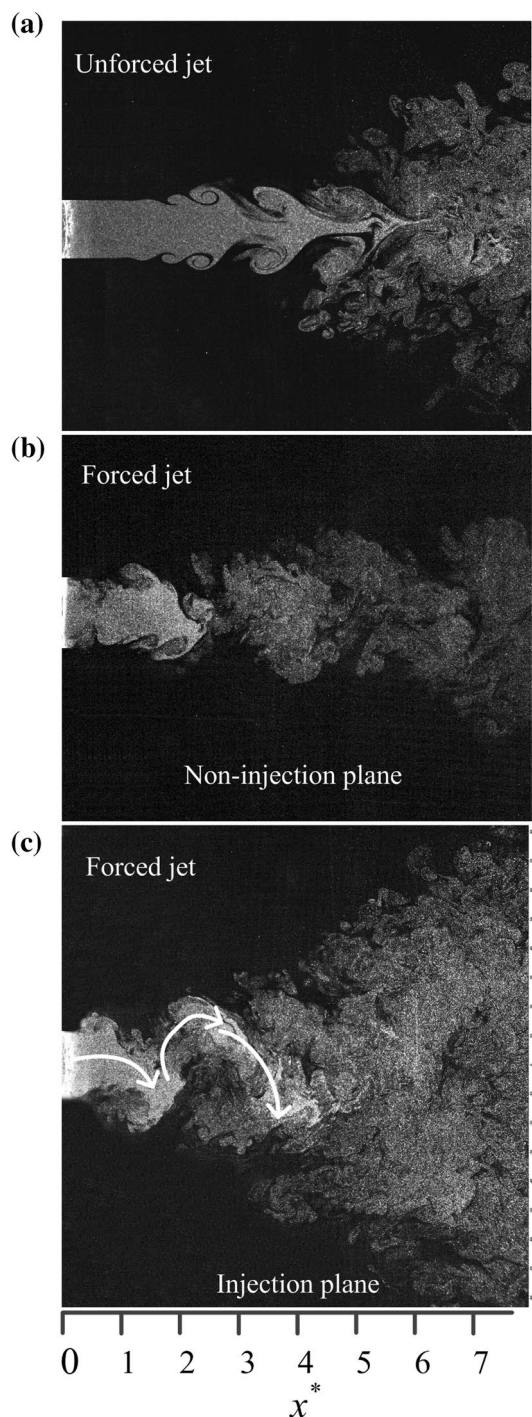


Fig. 11 Photographs from flow visualization of the unforced benchmark and the optimal actuation. Flow is from the left to right. Comparison in the typical flow structure between the uncontrolled jet (a) and the controlled jet ($C_m = 1.2\%$, $f_e = 67$ Hz, DC = 7%) in the non-injection (b) and injection planes (c)

by 6 arrows in Fig. 10. In other words, the mechanisms of MLC for open- and closed-loop control are similar.

Figure 11 shows typical photographs in the injection (x, z) and non-injection (x, y) planes. The unforced jet (Fig. 11a)

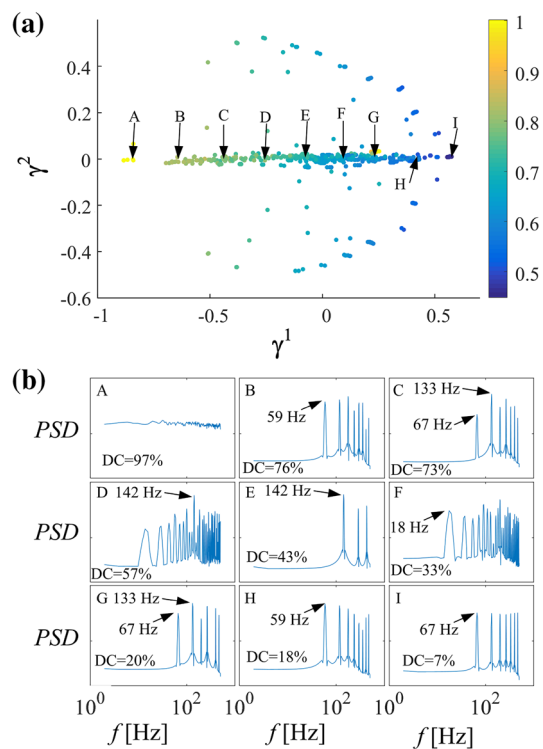


Fig. 12 Proximity map of MLC with multi-frequency forcing in analogy to Fig. 8. For details see text

is, by symmetry, similar in both planes. The smoke clearly distills high-frequency shear-layer vortices which are consistent with the observed 135 Hz shear-layer signal of Fig. 6a. Further visualizations in the (y, z) plane (not shown here) are consistent with axisymmetric ring vortices. Figure 11b, c show the flow visualization data under the optimal periodic forcing (15). The photograph in the injection plane displays a strong flapping motion which leads to large dispersion of smoke in the transverse direction. That in the non-injection plane indicates no increase in the transversal mixing. Yet, the photographs in both planes indicate that the length of the potential core is about $2D$. This value is to be compared with the continuous smoke on the centerline until at least 4 diameters for the unforced jet. These observations are consistent with the observed decrease of the chosen cost function. This flapping, characterized by greatly enhanced entrainment in the non-injection plane and very rapid spread in the injection plane, has also been observed in Yang et al. (2016). In their study, the jet manipulation was performed with two asymmetrically arranged unsteady minijets. All results convincingly demonstrate that the flapping motion is responsible for the rapid decay of the centreline mean velocity (Fig. 11).

Similarly to Sect. 4, the control landscape is given in Fig. 12a. Figure 12b shows the power spectral density functions for selected control laws A–I. The coordinate γ^1 is

strongly correlated to DC . From A to I , the DC varies from 97% (left) to 7% (right), while the cost J decreases from 1 to 0.458. The optimal law b_{opt} is indexed by I . These results indicate again that DC plays an important role in control performance.

6 Discussion of open versus closed-loop control

Sections 4 and 5 reveal arguably surprising features of machine learning control and of the optimal actuation mechanism. In the following, we present three aspects: the learning rate for periodic forcing (Sect. 6.1), the poor performance of feedback control (Sect. 6.2) and the convergence against pure periodic forcing without other frequency components (Sect. 6.3).

6.1 Learning rate of MLC for optimal periodic forcing

In Sect. 5, MLC performs a global search over many frequencies and many duty cycles and arrives at pure periodic forcing after testing only 400 individuals. From this and the previous study (Wu et al. 2016), the characterizing

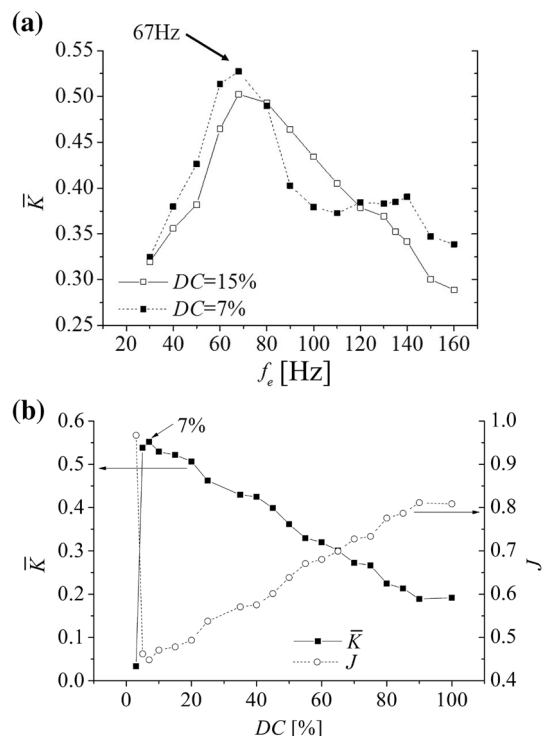


Fig. 13 Performance of periodic forcing. **a** The dependence of \bar{K} on f_e at $Re_D = 8000$, $C_m \approx 1.2\%$. **b** The dependence of \bar{K} on DC at $Re_D = 8000$, $C_m = 1.2\%$ and $f_e = 67$ Hz

frequency and duty cycle of this periodic forcing could not be improved further by a systematic search.

Moreover, the decay rate \bar{K} is 8% larger as compared to the previously achieved mixing, where DC was fixed at 15% and C_m and f_e were optimized using a dual-input/single-output extremum-seeking controller (Wu et al. 2018), yielding $C_m = 1.2\%$ and $f_e = 67$ Hz (see Fig. 13a, $DC = 15\%$). The MLC-optimized open-loop actuation is strictly periodic. The control law (15) contains only the excitation frequency h_4 . This frequency is the same as $f_e = 67$ Hz as identified by Fan et al. (2017). Note that $f_e = f_0/2$, i.e. half the unforced shear-layer frequency. The improved control performance is predominantly caused by DC which is reduced to 7% when MLC is employed. The optimality of DC at fixed excitation frequency is demonstrated in Fig. 13b.

The maximum exit velocity of the minijet and, hence, its penetration depth depends on both C_m and DC . For a given C_m , the penetration depth is inversely correlated with DC . A DC of 7% at fixed excitation frequency yields the maximum jet exit velocity under ambient conditions (see Fig. 2) and also yields the maximum decay rate of the main jet (see Fig. 13b). These results indicate that the DC of 7% has the maximum impulse to affect the main jet giving rise to the maximum \bar{K} value. Another evidence is given in Fig. 14 which shows the influence of minijet on jet exit profile. With a fixed C_m , a smaller DC yields larger changes of the main jet, especially for the standard deviation $u_{r.m.s.}$. Therefore, MLC eventually chooses the small DC (7%) in the best control law. Note that the employed electromagnetic-valves do not open when the DC is less than 5%. Thus, the \bar{K} drops dramatically from 0.538 at $DC = 5\%$ to 0.033 at $DC = 3\%$.

This performance can be considered quite impressive for an evolutionary learning algorithm. These algorithms are powerful for exploration but perform less well for exploitation, the realm of gradient-based parameter optimization.

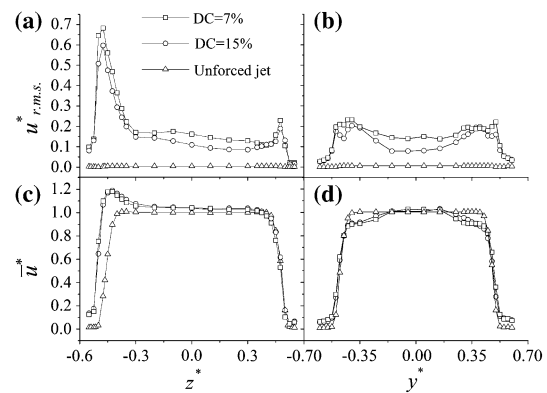


Fig. 14 Optimal periodic forcing: radial distribution of **a**, **b** turbulent intensity $u^*_{r.m.s.} = u_{r.m.s.}/U_j$ and **c**, **d** $\bar{u}^* = \bar{u}/U_j$ at $x^* = 0.05$ of the unforced jet and manipulated jet at $DC = 7\%$ and $DC = 15\%$ in $x - z$ (**a**, **c**) and $x - y$ plane (**b**, **d**), $C_m = 1.2\%$ and $f_e = 67$ Hz

Moreover, 400 individuals to convergence may be compared with a systematic parameter variation over two parameters. Let us assume 400 cost functions are evaluated with a systematic equidistant sampling using 20 frequencies in the range from 0 to 200 Hz and 20 duty cycles from zero to unity. The closest result $f_c = 60$ Hz and $DC = 10\%$ differs from the optimal parameters. The difference in DC and frequency yields a noticeably worse performance as indicated in Fig. 13.

MLC may also be compared with local gradient search—at the expense of potentially arriving in a suboptimal minimum. A two-parameter extremum seeking and a two-parameter simplex search can be expected to require $O(100)$ test runs worth of measurement time. Summarizing, MLC is a competitive two-parameter optimizer, a task which is not a typical application of an evolutionary learning algorithm. In addition, MLC has operated in much larger search space of multi-frequency laws. A side benefit of this search is that the performance advantages of sensor-based feedback and of non-periodic actuation have been assessed.

6.2 No performance benefits of sensor-based feedback

The performance of sensor-based feedback is surprisingly low. In the following, we explore if sensor-based feedback $b = B(s_1, s_2, s_3, s_4)$ could have mimicked the best open-loop control. The MLC feedback law $b = B_{\text{opt}}(s_3)$ employs only s_3 , i.e. the velocity fluctuation at $x = 3D$. Based on Fig. 7, we also include the fluctuation at $x = 5D$ in the analyzed control

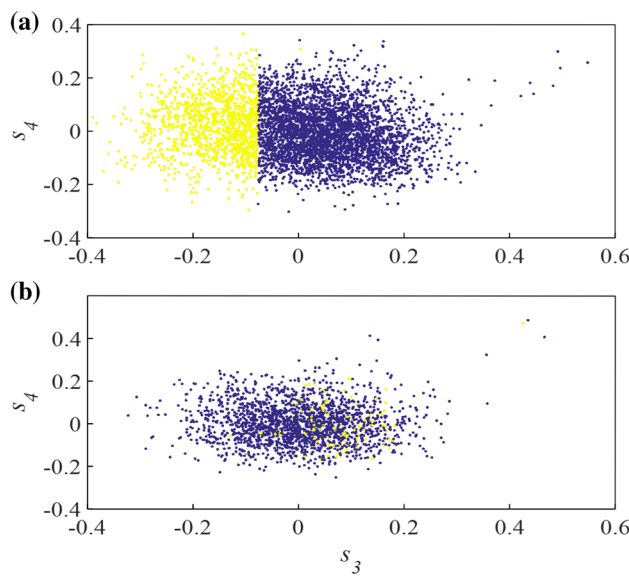


Fig. 15 Analysis of the optimal MLC-based open-loop (a) and closed-loop control (b). Both figures show measured sensor signals s_3 and s_4 and indicate the forcing with solid yellow bullets for actuation and blue bullets for the off-phase

law $b = B(s_3, s_4)$, ignoring s_1 and s_2 on grounds that they are hardly used in later MLC generations. Figure 15 shows the actuation b at measured sensor signals s_3 and s_4 both, for MLC-based open- and closed-loop actuation. Figure 15a shows clearly the s_3 -dependent ‘firing’ criteria. However, in Fig. 15b, the optimal periodic forcing seems hardly to be correlated with s_3 and s_4 . The ON and OFF actuation phases appear statistically distributed over the whole data region. This mixing of two actuation states strongly indicates that the optimal periodic forcing cannot be found by the ansatz $b = B(s_3, s_4)$.

Effectively, the closed-loop strategy is based on phasor control assuming an oscillatory flow. The peculiarity of this experiment is the observed best mixing for a short ‘firing’ window—complicated by large cycle-to-cycle variations from turbulence, as indicated in Figs. 6 and 10. If these cycle-to-cycle variations significantly contribute to mixing performance, a feedback based on phasor feedback of oscillatory flow cannot be expected to be more effective. Otherwise, the cycle-to-cycle variation may be filtered out by varying the sensor positions and by filtering the sensor signals, e.g. a long-tailed Morlet filter (Bourgeois et al. 2013). We observed small improvements of feedback with variations of the hotwire position and with Morlet filtering, yet did not get close to the best periodic forcing. Future investigations are needed to assess if feedback can beat the best periodic forcing with hardware and software optimization.

The ON/OFF actuation with small duty cycles makes the presented optimal jet mixing different from other experimental turbulence control studies where in-time phasor control has outperformed working periodic forcing (Pastoor et al. 2008). Moreover, the ON/OFF actuation leaves little room for a slow parameter adaption. However, there were also cases in which the optimal high-frequency forcing has outperformed MLC-based sensor-based feedback (Li et al. 2017; Parezanović et al. 2016). This is not surprising as the signal-to-noise ratio of high-frequency actuation effects versus broadband frequency distribution tends to be very poor. In Li et al. (2017) only one of 16 pressure sensors was able to resolve the actuation frequency and its phase, but only with a two period delay.

Following Li et al. (2017), we have also explored generalized control laws $b = B(s_1, \dots, s_4, h_1, \dots, h_9)$, i.e. Eq. (8), comprising sensor-based feedback and multi-frequency forcing. This ansatz has increased the convergence time of MLC and also yielded the same periodic forcing.

6.3 No performance benefits from multi-frequency forcing

Literature contains many experimental flow control studies in which multi-frequency forcing has outperformed periodic forcing at the same or similar amplitude. In Li et al. (2017),

MLC has identified a two-frequency forcing which has improved the drag reduction of a car model as compared to optimized periodic forcing. In Chovet et al. (2017), a similar observation was made for the mixing enhancement behind a backward-facing step. Numerous reports show how sub- and subsubharmonic forcing components increase the mixing layer width by triggering more early vortex pairing (Coats 1997; Monkewitz 1988). Hence, the performance of pure periodic forcing for optimal jet mixing is initially surprising.

However, our actuation is tailored towards flapping forcing. Yet, axisymmetric and helical forcing also enhance jet entrainment. Paschereit et al. (1995), for instance, experimentally observes that a combination of harmonic and subharmonic maximizes initial shear-layer growth of a jet. In a numerical jet mixing study (Hilgers and Boersma 2001), a combination of axisymmetric and helical forcing is optimized. However, stability theory (Garnaud et al. 2013), computational studies (Koumoutsakos et al. 2001) and experiments (Henderson 2010) suggest that the jet-flapping mode is the most essential requirement for mixing enhancement. Yang et al. (2016) also found that an asymmetric excitation is more effective than a symmetric excitation since the former can generate an asymmetric flow structure that is more unstable. Thus, the current periodic forcing induced a strong asymmetric flapping of the jet in the injection plane which enhanced the jet spreading rate largely. Note that, the flapping motion of the controlled jet at $f_e/f_0 = 0.5$ is stronger as compared to other f_e/f_0 examined (Fan et al. 2017). This is a comparably simple mechanism, like the excitation of pendulum motion with a kick near the lower equilibrium point. It is difficult to perceive how scheduling the ‘firing’ non-periodically should improve such an inherently periodic phenomena. For mixing layer control, the multi-frequency forcing enhances the vortex merging process and can effectively control the number of merging vortices, and thus the growth of a mixing layer (Coats 1997; Inoue 1992). For jet mixing enhancement, flapping and shear-layer vortices are strongly interwoven (Garnaud et al. 2013) and strongly susceptible to forcing at a single frequency. From the far-field measurements, the flapping jet is notable different from bifurcating and blooming jets (Reynolds et al. 2003): only a single maximum of the time-averaged streamwise velocity is observed (Fan et al. 2017).

7 Conclusions

In this experimental study, we maximize jet mixing using one minijet actuator and two hotwire sensors—advancing past closed-loop control studies by the group (Wu et al. 2016). The control law ansatz comprises a multi-frequency forcing, sensor-based feedback and combinations thereof following Li et al. (2017). From this large search space,

machine learning control (MLC) has identified periodic forcing with short duty cycle as optimal. The mixing is quantified by the averaged streamwise velocity decay rate at five diameters downstream on the symmetry axis. The achieved mixing is better than that in a previous study by Wu et al. (2016) with extremum seeking control since a better (smaller) duty cycle was found. MLC performed optimization in only 4 generations with 100 control laws in each, i.e. 400 runs with 5 s evaluation for each run. The frequency and duty cycle identified by MLC could not be improved further with parametric studies. Summarizing, the learning time is comparable to alternative optimization of periodic forcing, e.g. testing 50 different frequencies for 20 different duty cycles.

In addition to identifying the optimal periodic forcing, MLC indicates that neither additional forcing frequencies nor employing sensor-based feedback improves mixing further. Both implications may initially be surprising but can—in hindsight—easily be explained. Numerous turbulence control experiments show how multi-frequency forcing outperforms periodic forcing. In Li et al. (2017), MLC identified that multi-frequency forcing is more effective for drag reduction of a car model than the optimized periodic forcing. MLC also found multi-frequency forcing to outperform optimized periodic actuation in the reduction of a recirculation zone behind a backward facing step (Chovet et al. 2017). The list of similar observations can easily be extended (Coats 1997). Multi-frequency forcing is a very large superset of periodic forcing. In case of jet mixing, the underlying mechanism is a flapping in the plane containing the minijet. It seems that this simple mechanism cannot be improved by other frequencies. Moreover, a single actuator may not trigger other mechanisms which may be based on other different frequencies.

The poor performance of sensor-based feedback for an oscillatory mechanism is also initially surprising in light of a common experience of turbulence control experiments: If periodic forcing improves a performance, feedback can generally improve it further. This feedback may adjust in-time the phase of actuation to flow events (Pastoor et al. 2008) or may perform a slow adaption of a forcing parameter. However, in case of the jet mixing neither phasor control nor parameter adaption can be expected to work. The mixing is critically depending on a short ‘firing’ time in a narrow time interval. Any feedback ‘firing’ policy will be mitigated by the low-frequency drifts and by high-frequency noise. In addition, the boolean on-off nature of control excludes the possibility of an amplitude adaptation. In hindsight, the poor performance of sensor-based feedback in comparison with the optimal periodic forcing can be expected if very short duty cycles are necessary for good actuation performance. We did improve sensor-based feedback by several measures, e.g. optimization of the sensor position or other

sensor filters. However, in none of these experiments the performance of periodic forcing has been reached.

The current jet mixing study reveals that a simple periodic actuation appears to be best. MLC simultaneously optimizes the forcing parameters at a highly competitive learning rate and seems to exclude performance increases by feedback and new frequencies. Subsequent studies of the authors concern jet mixing enhancement in the same facility, but employing all six minijets. MLC has a large untapped potential in turbulence control applications. We actively pursue a MLC generalization which learns not only the optimal control law but also the corresponding control-oriented model within few hundred or few thousand short test runs.

Acknowledgements This work is supported by a public Grant overseen by the French National Research Agency (ANR) as part of the “Investissement d’Avenir” program, through the “iCODE Institute project” funded by the IDEX Paris-Saclay, ANR-11-IDEX-0003-02, by the ANR Grants ‘ACTIV_ROAD’ and ‘FlowCon’. The thesis of RL is supported by the OpenLab Fluidics between PSA Peugeot-Citroën and Institute Pprime (Fluidics@poitiers). The financial support of NSFC via Grant (approval no. 91752109) is acknowledged. We appreciate valuable stimulating discussions with Steven Brunton, Camila Chovet, Eurika Kaiser, Laurent Keirnsbulck, Nathan Kutz, Richard Semaan and the French-German-Canadian-American pinball team: Guy Yoslan Cornejo-Maceda, Nan Deng, François Lusseyran, Robert Martinuzzi, Cedric Raibaud and Luc Pastur.

References

- Becker R, King R, Petz R, Nitsche W (2007) Adaptive closed-loop control on a high-lift configuration using extremum seeking. *AIAA J* 45(6):1382–92
- Bourgeois JA, Martinuzzi RJ, Noack BR (2013) Generalised phase average with applications to sensor-based flow estimation of the wall-mounted square cylinder wake. *J Fluid Mech* 736:316–350
- Brackston RD, Wynn A, Morrison JF (2016) Extremum seeking to control the amplitude and frequency of a pulsed jet for bluff body drag reduction. *Exp Fluids* 57(10):article 159 (1–14)
- Bradbury LJS, Khadem AH (1975) The distortion of a jet by tabs. *J Fluid Mech* 70(04):801–813
- Brameier M, Banzhaf W (2007) Linear genetic programming. Springer, Berlin
- Brunton SL, Noack BR (2015) Closed-loop turbulence control: progress and challenges. *Appl Mech Rev* 67(5):050,801:01–48
- Choi H, Jeon WP, Kim J (2008) Control of flow over a bluff body. *Ann Rev Fluid Mech* 40:113–139
- Chovet C, Keirnsbulck L, Noack BR, Lippert M, Foucaut JM (2017) Machine learning control for experimental shear flows targeting the reduction of a recirculation bubble. In: The 20th World Congress of the International Federation of Automatic Control (IFAC). Toulouse, France, pp 1–4
- Coats C (1997) Coherent structures in combustion. *Prog Energy Combust Sci* 22:427–509
- Collis SS, D JR, Seifert A, Theofilis V (2004) Issues in active flow control: theory, control, simulation, and experiment. *Prog Aerosp Sci* 40:237–289
- Davis MR (1982) Variable control of jet decay. *AIAA J* 20(5):606–609
- Dracopoulos DC, Kent S (1997) Genetic programming for prediction and control. *Neural Comput Appl* 6:214–228
- Duriez T, Brunton SL, Noack BR (2016) Machine learning control—taming nonlinear dynamics and turbulence. *Fluid mechanics and its applications*. Springer, Berlin
- Fan DW, Wu Z, Yang H, Li JD, Zhou Y (2017) Modified extremum-seeking closed-loop system for jet mixing enhancement. *AIAA J* 55(11):3891–3902
- Freund JB, Moin P (2000) Jet mixing enhancement by high-amplitude fluidic actuation. *AIAA J* 38(10):1863–1870
- Garnaud X, Lesshaft L, Schmid PJ, Huerre P (2013) The preferred mode of incompressible jets: linear frequency response analysis. *J Fluid Mech* 716:189–202
- Gutmark E, Grinstein F (1999) Flow control with noncircular jets. *Ann Rev Fluid Mech* 31(1):239–272
- Henderson B (2010) Fifty years of fluidic injection for jet noise reduction. *Int J Aeroacoust* 9(1–2):91–122
- Hilgers A, Boersma BJ (2001) Optimization of turbulent jet mixing. *Fluid Dyn Res* 29:345–368
- Ho CM, Gutmark E (1987) Vortex induction and mass entrainment in a small-aspect-ratio elliptic jet. *J Fluid Mech* 179:383–405
- Hussain F, Husain HS (1989) Elliptic jets. Part 1. Characteristics of unexcited and excited jets. *J Fluid Mech* 208:257–320
- Inoue O (1992) Double-frequency forcing on spatially growing mixing layers. *J Fluid Mech* 234:553–581
- Johari H, Pacheco-Tougas M, Hermanson J (1999) Penetration and mixing of fully modulated turbulent jets in crossflow. *AIAA J* 37(7):842–850
- Kaiser E, Li R, Noack BR (2017) On the control landscape topology. The 20th World Congress of the International Federation of Automatic Control (IFAC). Toulouse, France, pp 1–4
- Koumoutsakos P, Freund J, Parekh D (2001) Evolution strategies for automatic optimization of jet mixing. *AIAA J* 39(5):967–969
- Lee C, Kim J, Babcock D, Goodman R (1997) Application of neural networks to turbulence control for drag reduction. *Phys Fluids* 9(6):1740–1747
- Li R, Noack BR, Cordier L, Borée J, Harambat F (2017) Drag reduction of a car model by linear genetic programming control. *Exp Fluids* 58(article 103):1–20
- Mardia KV, Kent JT, Bibby JM (1979) Multivariate analysis. Probability and mathematical statistics. Academic Press, Cambridge
- Maury R, Koenig M, Cattafesta L, Jordan P, Delville J (2012) Extremum-seeking control of jet noise. *Int J Aeroacoust* 11(3–4):459–473
- Mi J, Kalt P, Nathan G, Wong C (2007) Piv measurements of a turbulent jet issuing from round sharp-edged plate. *Exp Fluids* 42(4):625–637
- Monkewitz P (1988) Subharmonic resonance, pairing and shredding in the mixing layer. *J Fluid Mech* 188:223–252
- Noack BR (2018) Closed-loop turbulence control—from human to machine learning (and retour). In: Zhou Y, Kimura M, Peng G, Lucey A, Huang L (eds) *Fluid-structure-sound interactions and control*. FSSIC 2017. Springer, Singapore, pp 23–32
- Parezanović V, Cordier L, Spohn A, Duriez T, Noack BR, Bonnet JP, Segond M, Abel M, Brunton SL (2016) Frequency selection by feedback control in a turbulent shear flow. *J Fluid Mech* 797:247–283
- Paschereit CO, Wygnanski I, Fiedler HE (1995) Experimental investigation of subharmonic resonance in an axisymmetric jet. *J Fluid Mech* 283:365–407
- Pastoor M, Henning L, Noack BR, King R, Tadmor G (2008) Feedback shear layer control for bluff body drag reduction. *J Fluid Mech* 608:161–196
- Rapoport D, Fono I, Cohen K, Seifert A (2003) Closed-loop vectoring control of a turbulent jet using periodic excitation. *J Propul Power* 19(4):646–654
- Reynolds W, Parekh D, Juvet P, Lee M (2003) Bifurcating and blooming jets. *Ann Rev Fluid Mech* 35(1):295–315

- Samimy M, Kim JH, Kastner J, Adamovic I, Utkin Y (2007) Active control of high-speed and high-Reynolds-number jets using plasma actuators. *J Fluid Mech* 578:305–330
- Wahde M (2008) Biologically inspired optimization methods: an introduction. WIT Press, Ashurst
- Wiltse JM, Glezer A (1993) Manipulation of free shear flows using piezoelectric actuators. *J Fluid Mech* 249:261–285
- Wu Z, Wong CW, Wang L, Lu Z, Zhu Y, Zhou Y (2015) A rapidly settled closed-loop control for airfoil aerodynamics based on plasma actuation. *Exp Fluids* 56(8):article 158 (1–15)
- Wu Z, Zhou Y, Cao HL, Li WL (2016) Closed-loop enhancement of jet mixing with extremum-seeking and physics-based strategies. *Exp Fluids* 57:1–14
- Wu Z, Wong CW, Zhou Y (2018) Dual-input/single-output extremum-seeking system for jet control. *AIAA J* 56(4):1463–1471
- Yang H, Zhou Y (2016) Axisymmetric jet manipulated using two unsteady minijets. *J Fluid Mech* 808:362–396
- Yang H, Zhou Y, So R, Liu Y (2016) Turbulent jet manipulation using two unsteady azimuthally separated radial minijets. *Proc R Soc A* 472(2191):20160,417
- Zaman KBM, Hussain AKMF (1980) Vortex pairing in a circular jet under controlled excitation. Part 1. General jet response. *J Fluid Mech* 101(3):449–491
- Zaman KBM, Reeder MF, Samimy M (1994) Control of an axisymmetric jet using vortex generators. *Phys Fluids* 6(2):778–793
- Zhang MM, Cheng L, Zhou Y (2004a) Closed-loop control of fluid-structure interactions on a flexibly supported cylinder. *Eur J Mech B* 23:189–197
- Zhang MM, Cheng L, Zhou Y (2004b) Closed-loop-controlled vortex shedding and vibration of a flexibly supported square cylinder under different schemes. *Phys Fluids* 16(5):1439–1448
- Zhou Y, Du C, Mi J, Wang XW (2012) Turbulent round jet control using two steady minijets. *AIAA J* 50(3):736–740

Publisher's Note Springer Nature remains neutral with regard to jurisdictional claims in published maps and institutional affiliations.

Affiliations

Zhi Wu^{1,2}  · Dewei Fan^{1,2} · Yu Zhou^{1,2} · Ruiying Li³ · Bernd R. Noack^{1,4,5}

 Yu Zhou
yuzhou@hit.edu.cn

 Bernd R. Noack
Bernd.Noack@limsi.fr

¹ Institute for Turbulence-Noise-Vibration Interaction and Control, Harbin Institute of Technology, Shenzhen Campus, Shenzhen, People's Republic of China

² Digital Engineering Laboratory of Offshore Equipment, Shenzhen, People's Republic of China

³ Institut PPRIME, CNRS-Université de Poitiers-ISAE-ENSMA, 86962 Futuroscope Chasseneuil, France

⁴ LIMSI-CNRS, Rue John von Neumann, Campus Universitaire d'Orsay, Bât 508, 91403 Orsay, France

⁵ Institut für Strömungsmechanik und Technische Akustik (ISTA), Technische Universität Berlin, Müller-Breslau-Straße 8, 10623 Berlin, Germany